Topological structures of the resistive pressure gradient turbulence with averaged poloidal flow

B.A. Carreras[1], I. Llerena Rodríguez[2] and L. García[1]

[1] Departamento de Física, Universidad Carlos III de Madrid, Avda. de la Universidad 30, 28911 Leganés, Madrid, Spain
[2] Departament d'Àlgebra i Geometria, Facultat de Matemàtiques, Universitat de Barcelona, Gran Via de les Corts Catalanes, 585, 08007 Barcelona, Spain

E-mail: bacarreras@gmail.com, illerena@ub.edu and lgarcia@fis.uc3m.es

Abstract. When a significant averaged poloidal flow is generated by the resistive pressure-gradient-driven turbulence the topological properties of the flow structures can change in some radial regions where the shear flow is large. We have applied the topological analysis approach that we have developed [2013 *J. Phys. A: Math. Theor.* **46** 375501] to this situation and found that in addition to the filamentary vortex structures there are deformed toroidal structures that seem to act as transport barriers. Analysis of all these structures is presented here.

PACS numbers: 52.35.Ra, 52.65.Kj, 47.27.-i

1. Introduction

In trying to understand transport in magnetically confined plasmas, we have used the continuous time random walk (CTRW) approach [1]. This requires the characterisation of trapping and flights of particles. In our previous studies [2], we have shown the role of the plasma vortices in the particle trapping and we have applied [3] a topological approach in understanding the properties of these flow structures. This analysis was done for turbulence calculations that did not include an averaged poloidal flow. By allowing for a break in the up-down symmetry of the electrostatic potential, a self-consistent averaged poloidal flow is generated by the turbulence. The flow level depends of the viscous damping effects. Here we discuss the impact of the presence of the averaged poloidal flow on the topological structures of the overall turbulent flow.

The inclusion of the averaged poloidal flow in the calculations of the pressure-gradient-driven turbulence decreases the level of turbulence-induced particle transport. It also changes the topological structure of the flow in some radial locations and increases the types of particle trapping.

When the averaged poloidad flow is not included, the electrostatic potential has the symmetry property $\Phi(r, -\theta, -\zeta) = -\Phi(r, \theta, \zeta)$, as we discuss in section 2. In this case, the flow structures are characterised by their filamentary nature of the flow vortices, which are linked to the corresponding singular surfaces. These flow structures can be correlated with the Fourier components of the electrostatic potential Φ and they have the topological structure of a toroidal knot with poloidal and toroidal mode

numbers, m and n respectively, corresponding to the helicity associated with the component.

In the case that an averaged poloidal flow is self-consistently included in the calculation, some of the topological structures of the turbulent flow mentioned before still remain. However, there are some new structures, they still have the topological structure of a toroidal knot but are not necessarily associated with the m and n values of the associated Fourier component. They are associated with the transport barriers created by the shear in the mean flow.

Here we discuss this new structures and we investigate how the statistical characterisation of the different structures in Ref [3] may change with the inclusion of the global flow.

The rest of the paper is organised as follows. In section 2, we discuss the basic turbulence model that we use for the calculations presented in this paper. In section 3, we present the numerical results comparing the solutions with averaged poloidal flow with the ones without the flow. In section 4, we summarise the methods used in analysing the topology of the flow. In section 5, we discuss the new flow structures that emerge when the averaged poloidal flow is included. The radial change of these structures is discussed in section 6. A comparative analysis of the statistical quantification of the structures is given in section 7. Particle trapping in the structures is discussed in section 8. Finally the conclusions of this paper are presented in section 9.

sec:PlasmaModel

2. Plasma turbulence model

The present calculations of plasma turbulence are based on the set of reduced magnetohydrodynamic (MHD) equations [4] with a pressure gradient drive [5]. The geometry is that of a periodic cylinder, with minor radius a and length $L_0 = 2\pi R_0$. We use a coordinate system (r, θ, ζ), in which r is the radius of the cylindrical surface, θ is the poloidal angle, and $\zeta = z/R_0$, where z is the coordinate along the axis of the cylinder, so ζ is an effective toroidal angle when the cylinder is bent in a torus. In Ref. [6], these equations were simplified because the dynamics of the resistive pressure-gradient-driven turbulence can be described by the electrostatic approximation. This approximation is only valid well below the ideal instability threshold. In the electrostatic limit, we can neglect the time variation of the perturbed poloidal magnetic flux function and the parallel derivatives along the magnetic field lines can be taken along the unperturbed field lines. Under these assumptions, the system of equations consists of a vorticity equation

$$m_i n_i \frac{\mathrm{d}\tilde{U}}{\mathrm{d}t} = -\frac{\nabla_\parallel^2 \tilde{\Phi}}{\eta} - \frac{\kappa}{B_0}\frac{1}{r}\frac{\partial \tilde{p}}{\partial \theta} + m_i n_i \hat{\mu} \nabla_\perp^2 \tilde{U}, \tag{1}$$

eq:U

and an equation of state,

$$\frac{\mathrm{d}p}{\mathrm{d}t} = D_\perp \nabla_\perp^2 \tilde{p} + D_\parallel \nabla_\parallel^2 \tilde{p}. \tag{2}$$

eq:pr

Here, $\mathrm{d}/\mathrm{d}t = \partial/\partial t + \mathbf{V}_\perp \cdot \nabla$ is the convective derivative; the perpendicular component of the velocity is $\mathbf{V}_\perp = -\nabla_\perp \Phi \times \mathbf{z}/B_0$; $U = \mathbf{z} \cdot \nabla \times \mathbf{V}_\perp / B_0$ is the z-component of the vorticity; Φ is the electrostatic potential; m_i is the ion mass; n_i is the ion density; p is the pressure; η is the resistivity; $\hat{\mu}$ is the kinematic viscosity; $\nabla_\parallel$ is the derivative along the magnetic field; and κ is the averaged magnetic field curvature. The magnetic field

is expressed as $\mathbf{B} = B_0\mathbf{z} + (\mathbf{z} \times \nabla\psi)/R_0$, where B_0 is the toroidal field, and ψ is the poloidal flux. The derivative along the magnetic field is then

$$\nabla_\parallel = \frac{\partial}{\partial\zeta} - \frac{1}{q}\frac{\partial}{\partial\theta}, \tag{3}$$

where q is the safety factor.

In equations (1)-(2), a tilde identifies perturbed quantities. For the nonlinear calculations, the effect of the $V_\parallel$ evolution in the dynamics of the resistive pressure-gradient-driven turbulence is replaced by a parallel diffusivity in the pressure equation. Viscosity and perpendicular transport are also included in the equations to provide the energy sink needed to get steady-state turbulence.

The driving term of the resistive pressure driven instability is the pressure gradient in the bad curvature region, that is, the second term on the right-hand side (rhs) of Eq. (1). The first term on the rhs is the field line bending term, which is stabilising. The resistivity weakens this term and allows the instability to grow.

To study the effect of an averaged poloidal velocity on the turbulence, we use a property of these equations that allows finding solutions with and without the averaged poloidal velocity. As we have seen, in the framework of the reduced MHD equations, the plasma flow velocity is given in terms of the electrostatic potential Φ by the following relation:

$$\mathbf{V}_\perp = -\nabla_\perp\Phi \times \mathbf{z}/B_0. \tag{4}$$ Vperp

An equivalent velocity stream function is defined as $-\Phi/B$.

A particular solution of the system of equations (1)-(2) is given in term of the Fourier expansion of the two variables:

$$\Phi(r,\theta,\zeta,t) = \sum_{m,n} \Phi_{mn}(r,t)\sin(m\theta + n\zeta) \tag{5}$$

$$p(r,\theta,\zeta,t) = \sum_{m,n} p_{mn}(r,t)\cos(m\theta + n\zeta) \tag{6}$$

This solution has the symmetry property

$$\Phi(r,-\theta,-\zeta) = -\Phi(r,\theta,\zeta) \tag{7}$$ sym

Using this expansion, the poloidal and toroidal angle averaged of electrostatic potential is zero and so the corresponding averaged poloidal velocity. When we allow for the generation of an average poloidal velocity in the calculation, we use the following Fourier expansions:

$$\Phi(r,\theta,\zeta,t) = \sum_{m,n} \Phi^s_{mn}(r,t)\sin(m\theta + n\zeta) + \sum_{m,n} \Phi^c_{mn}(r,t)\cos(m\theta + n\zeta) \tag{8}$$

$$p(r,\theta,\zeta,t) = \sum_{m,n} p^s_{mn}(r,t)\sin(m\theta + n\zeta) + \sum_{m,n} p^c_{mn}(r,t)\cos(m\theta + n\zeta) \tag{9}$$

In this case, the averaged poloidal flow velocity, $\langle V_\theta\rangle$, is essentially given by

$$\langle V_\theta\rangle = \frac{1}{B_0}\frac{\mathrm{d}\Phi^c_{00}}{\mathrm{d}r}. \tag{10}$$

The poloidal flow profile evolution equation is derived by taking the flux surface average of the poloidal momentum balance equation,

$$\frac{\partial \langle V_\theta \rangle}{\partial t} = -\frac{1}{r^2}\frac{\partial}{\partial r}\left(r^2 \left\langle \tilde{V}_r \tilde{V}_\theta \right\rangle\right) - \mu \langle V_\theta \rangle \tag{11}$$

eq:Vth

Here the angular brackets, $\langle\ \rangle$, indicate the poloidal and the toroidal angle average over a magnetic flux surface and μ is the averaged flow damping caused by the magnetic pumping.

In the nonlinear calculations, we also include the evolution of the averaged pressure gradient. The corresponding equation is obtained by simply averaging Eq. (2),

$$\frac{\partial \langle p \rangle}{\partial t} = -\frac{1}{r}\frac{\partial}{\partial r}\left(r \left\langle \tilde{V}_r \tilde{p} \right\rangle\right) + \frac{1}{r}\frac{\partial}{\partial r}\left[rD_0 \frac{\partial \left(\langle p \rangle - p_{eq}\right)}{\partial r}\right] + Q, \tag{12}$$

eq:prav

where a source term Q is added to Eq. (12) to balance the energy losses.

To control the amount of averaged poloidal flow, we vary the value of the viscosity coefficient μ for the averaged flow. In what follows we will consider the results for a case without averaged poloidal velocity and two cases with averaged poloidal velocity for $\mu = 50\tau_R^{-1}$ and $\mu = 5\tau_R^{-1}$.

The plasma considered here is a model of a configuration of the Large Helical Device (LHD) [7]. The configuration has bad averaged curvature, which we model by

$$\kappa = 0.296r + 1.712r^3 + 4.854r^5 + 5.936r^7, \tag{13}$$

the equilibrium pressure profile is modeled by

$$p_{eq} = (1 - r^4)\left(1 - \frac{r^2}{2}\right), \tag{14}$$

and the q profile by

$$q = 2.726 - 3.3r^2 + 1.7r^4 - 0.48r^6. \tag{15}$$

In these expressions and from now on, the radius r is normalised to the minor radius a.

The main parameters of the nonlinear calculation are: $\beta_0 = 0.0044$, the inverse aspect ratio $\varepsilon = a/R_0 = 0.163$ and the Lundquist number $S = \tau_R/\tau_A = 10^5$. For these parameters, this configuration is unstable to resistive interchange modes. Here, β_0 is the ratio of the plasma pressure and the magnetic pressure at the plasma axis, $\beta_0 = 2\mu_0 p(0)/B_0^2$, τ_R is the resistive time, $\tau_R = \mu_0 a^2/\eta$, where η is constant, and τ_A is the Alfvén time, $\tau_A = R_0\sqrt{\mu_0 m_i n_i}/B_0$.

In the numerical calculations, we use the previously discussed Fourier expansion. A broad spectrum of modes is generated when the turbulence reaches a steady state. We included 3785 modes with m going up to $m = 85$. The radial grid is uniform and $\Delta r = 10^{-3}$.

3. Numerical results

sec:NumResults

Numerical results for the pressure-gradient-driven turbulence calculations have been discussed in previous publications [6]. In this paper, we will not go into those details. We will work with the numerical data when the calculation has reached the steady state. Here we will focus on the effect of the averaged poloidal flow on the turbulence by contrasting the results that have $\langle V_\theta \rangle \neq 0$ with the case with $\langle V_\theta \rangle = 0$.

In the turbulence calculations including the averaged velocity, once the steady state is reached the values of the average velocity change only slightly in time and its radial structure remains practically the same. This is shown in figure 1(a), where we have plotted the time-averaged profile of the Φ_{00} and the errors bars are the standard deviation due to the variation in time.

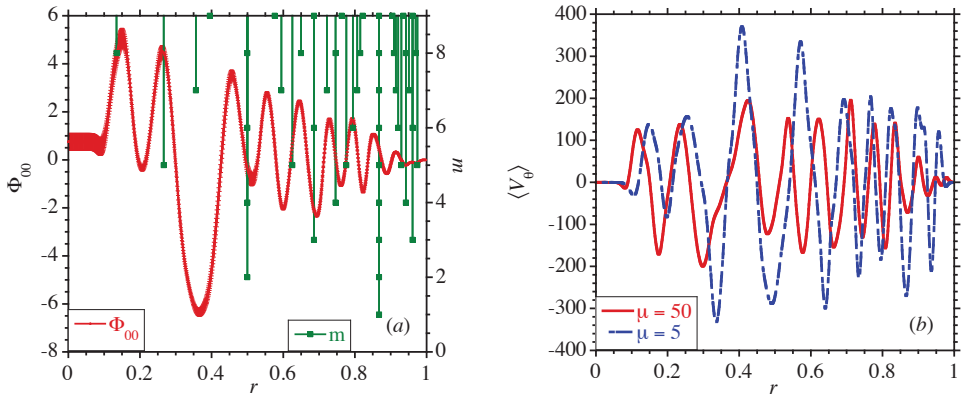

Figure 1. Radial dependence of the averaged poloidal flow: (a) time-averaged profile of the function Φ_{00} with the errors bars given by the standard deviation due to the variation in time, and (b) radial dependence of the averaged poloidal flow $\langle V_\theta \rangle$ for two different values of the viscosity. The location of the low order resonant surfaces m/n is also shown in (a).

FIG1

There is also relatively little change on the radial dependence of $\langle V_\theta \rangle$ when the viscosity is changed, as can be seen in figure 1(b). The peaks and valleys of the velocity profile are related to the positions of the low order resonant surfaces, as shown in figure 1(a).

The existence of radial zones with high shear flow causes the formation of multiple mini transport barriers that lead to a self-organisation of the averaged pressure profile. This may cause local steepening and flattening of the average pressure. Therefore, although the high shear flow in some radial regions reduces the level of the turbulent fluctuations, in other regions the local fluctuations may be enhanced.

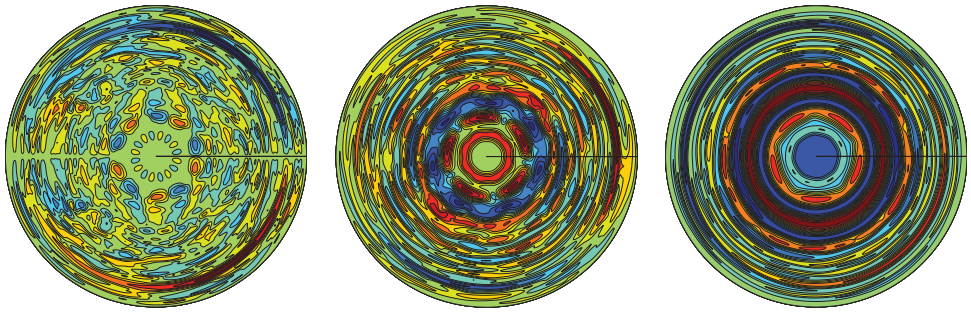

Figure 2. Contour plots of the function Φ for a $\zeta = 0$ toroidal cut and at a fixed time: (left) contour plots in the case of $\langle V_\theta \rangle = 0$, (middle) for $\langle V_\theta \rangle \neq 0$ with $\mu = 50\tau_R^{-1}$ and (right) for $\langle V_\theta \rangle \neq 0$ with $\mu = 5\tau_R^{-1}$.

FIG2

We can see the barrier formation from the Φ contour plots in figure 2. Figure 2

(left) shows the contour plots in the case of $\langle V_\theta \rangle = 0$. The contours show a chaotic pattern typical of turbulence. However, in the next two figures, for $\langle V_\theta \rangle \neq 0$ with $\mu = 50\tau_R^{-1}$ and $\mu = 5\tau_R^{-1}$, respectively, we see the emergence of circular contours that constraint the turbulent eddies and reduce their size.

The presence of these mini transport barriers allows for an overall improvement of confinement and we can see that the averaged gradient of pressure in the case with an averaged flow is higher than in the case without mean flow, in particular in the innermost region where the shear flow is largest. In figure 3, we have plotted the time averaged mean pressure profile for the three turbulence calculations considered here. The overall increase in the gradient is not obvious, the reason is that the heat sources have been reduced as the velocity increases to maintain similar levels of plasma internal energy (i.e. volume integral of the pressure). The source function Q has a Gaussian shape. For $\langle V_\theta \rangle \neq 0$ with $\mu = 50\tau_R^{-1}$ the coefficient of the Gaussian has been reduced to a 68% and for the case with $\mu = 5\tau_R^{-1}$ has been reduced to a 13% of the coefficient for the case without averaged poloidal flow.

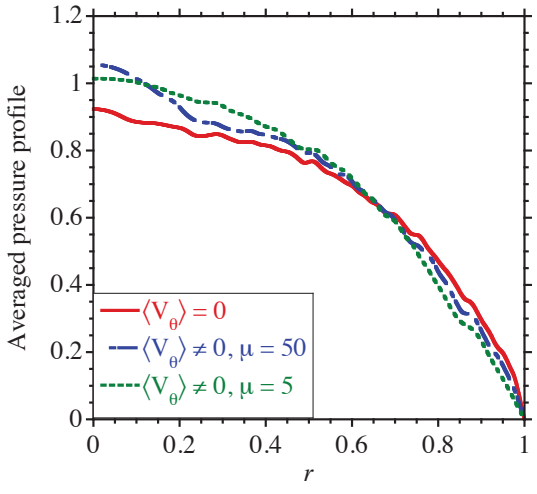

Figure 3. Time averaged mean pressure profile for the three turbulence calculations considered in this paper.

FIG3

4. Topological structures of the turbulent flow and their analysis

sec:Methods

All the information on the turbulence flow is contained in the electrostatic potential Φ, as can be seen from Eq. (4). For instance, the vortices of the turbulence can be easily identified by looking at the contours of the function Φ. We will study the topological structures of the turbulent flow using Φ.

We define a flow structure as the set of points such that $\Phi(\rho, \theta, \zeta, t) \geq \Phi_1$, for a suitable constant Φ_1. In Ref. [3], we looked at these flow structures in the case of an averaged poloidal flow $\langle V_\theta \rangle = 0$. We saw that they are filamentary. The filamentary structure is due to the vortices of the turbulence resonating with the low singular surfaces.

When $\langle V_\theta \rangle = 0$, the function Φ is symmetric, as indicated by Eq. (7). So, by changing the sign of the angles, the set $\Phi(\rho, \theta, \zeta, t) \geq \Phi_1$ is identical to the set

$\Phi(\rho,\theta,\zeta,t) \leq -\Phi_1$, and we only need to study one of these sets.

In this paper we deal with the case of an averaged poloidal flow $\langle V_\theta \rangle \neq 0$. Now, and due to the lack of symmetry of the function Φ, we need to look at a double structure: $\Phi(\rho,\theta,\zeta,t) \geq \Phi_1$ and $\Phi(\rho,\theta,\zeta,t) \leq -\Phi_1$.

We define Φ_0 as $\Phi_0 = \Phi_1/\mathrm{Max}\Phi$ with $\mathrm{Max}\Phi$ being the maximum value of Φ at time t. Therefore, Φ_0 gives a fraction of the maximum value of Φ and $0 < \Phi_0 < 1$. We have analysed the flow structures for a series of values of Φ_0. In general, structures are well defined for $\Phi_0 = 0.1$ and higher values. Above $\Phi_0 = 0.4$ very few structures remain, and the best interval for analysis is $[0.1, 0.2]$.

In order to have enough space resolution, we study the structures on 2-D radial slices, for a fixed radius r. It is advisable to take more resolution for the poloidal angle than for the toroidal angle. In each slice we take integer coordinates $(\theta,\zeta) \in [0, 2N) \times [0, N)$ and consider the two set of points

$$\begin{aligned} &\Phi(r, 2\pi\theta/2N, 2\pi\zeta/N, t) \geq \Phi_0 \mathrm{Max}\Phi \\ &\Phi(r, 2\pi\theta/2N, 2\pi\zeta/N, t) \leq \Phi_0 \mathrm{Min}\Phi \end{aligned} \tag{16}$$

eq:cubes

for constant values of r and t. For each time t, we take $2N$ values of r equally distributed in the interval $[0, 1]$. Here, we take for most of the results $N = 300$. In Ref. [3], we found this level of resolution to be good enough for these studies and there we described some of the convergence studies using different values of N.

For a given radius and time, we decompose each of the sets in equation (16) in its connected components. To define these components, we use 8-connectivity; i.e. the neighbours of every point (θ,ζ) are the eight points that touch one of its edges or corners: $(\theta \pm \{0,1\},\ \zeta \pm \{0,1\})$. For each component we want to know if it is a closed cycle and its helicity, or if it is an open filament and its length.

To carry a systematic study of each connected component we do a process of skeletonization or thinning consisting in reducing the foreground regions of the figure (binary image) without losing the homotopic properties of the structure, i.e. its connectivity, the number of loops and holes. For the skeletonization process we use an algorithm based on the hit-miss filter [8] which consists in detecting certain structural elements that allow us to eliminate a point without modify the homotopic properties of the set.

Reducing the components to its skeletons allow us to use graph algorithms for establishing if the component is a filament or a cycle, and computing the helicity in the case of cycles, and a measure of its length in the case of filaments. We take the number of points of the skeleton of the filaments as the measure of their length.

We can also calculate the life of cycles and filaments. This is done by intersecting the components of consecutive times. In the case with $\langle V_\theta \rangle = 0$, using a suitable time interval, the intersection of one component with the components in a consecutive time turns out to be void or over the 80% of the smaller of the two compared components. This allows to construct a graph which nodes are the components of a certain type, and the edges join a component with a component of the same type in next time, if they intersect. By following this graph, we determine the life times of the different flow structures. In the case with $\langle V_\theta \rangle \neq 0$ one must take into account the poloidal shift of the structures. In this case, an overlap of 60% or greater was used in identifying consecutive structures.

A detailed description of this analysis approach was presented in Ref. [3].

5. New flow structures in the case of an averaged poloidal flow

sec:Structures

We expect that the main effects of the averaged poloidal flow on the turbulence will happen in the regions of the large shear in the flow. In figure 4, we show an example of the relation between shear flow and Φ_{00} as a function of the radius. In this figure, we show only the lower half of radius because is the region where the averaged poloidal flow is largest and in this way we can see better the radial dependence. We see that in general maxima and minima of the shear flow correspond to minima and maxima of Φ_{00}. Therefore, in the region of high shear poloidal flow, we have high values of $|\Phi_{00}|$. This will have an impact on the flow structures.

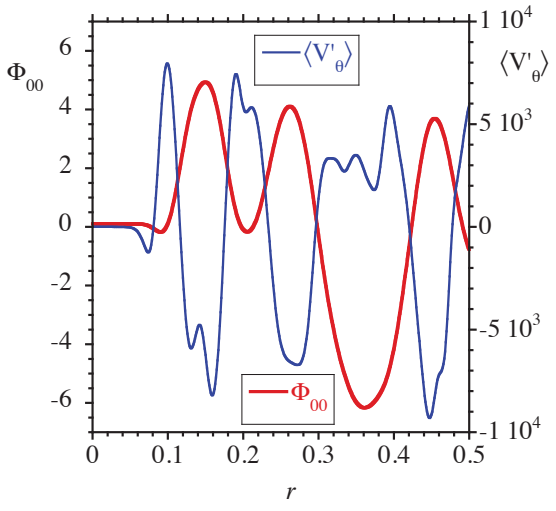

Figure 4. Φ_{00} and the radial derivative of the averaged poloidal flow as a function of the minor radius.

FIG4

Now, to see the impact on the flow structures of the large values of Φ_{00}, let us consider a simple 1-D example in which the electrostatic potential is only a function of the angle θ and it is simply given by

$$\Phi(\theta) = \Phi_{00} + \Phi_1 \sin(m\theta) \tag{17}$$

To study the topological structures we look at the points such that $\Phi(\theta) > c$ and $\Phi(\theta) < -c$, where c is a positive constant. For the case without average flow, $\Phi_{00} = 0$, and for an example with $m = 5$, the points we consider are above and below the two black lines in figure 5(a). In the first case, there is a clear up down symmetry and the filamentary nature appears clearly. In the second case, figure 5(b), there are points only on the top of the first black line. In this region we see that the set of points verifying the previous condition cover practically the whole line with small empty spaces where before were the filaments. Naturally, for this simplifying model, by selecting $c > 0.7$ we will see structures like the ones with no averaged flow. However, for the case of the function Φ, there are practically no points for this value of c.

In figure 6, we can see an example of these two types of structures as encountered in the turbulence calculations. In this figure we have plotted the connected component of the set of points for a fixed radius $r = 0.59$, where the averaged poloidal shear flow

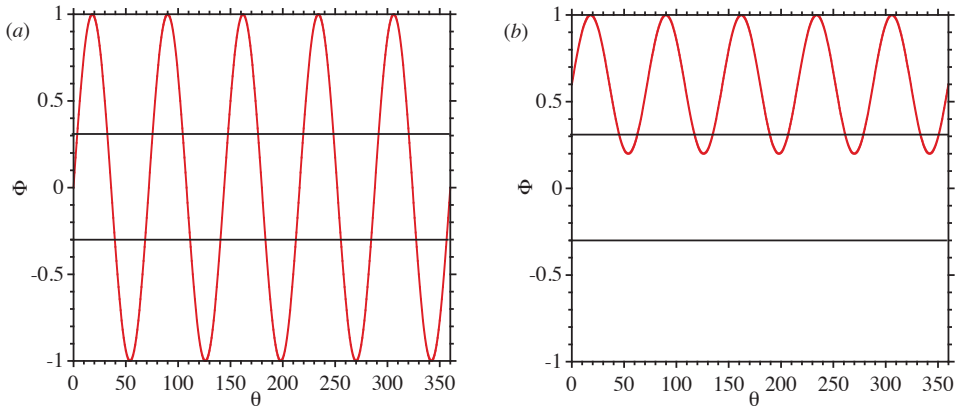

Figure 5. Representation of the simple model for the function Φ given by Eq. (16) for (a) a case with $\Phi_{00} = 0$ and (b) a case with $\Phi_{00} \neq 0$.

FIG5

is high and at a fixed time. Figure 6(a) corresponds to the case with no flow and figure 6(b) to the case with flow with $\mu = 50\tau_R^{-1}$. In figure 7, we have plotted the same two connected components in a 3-D plot to give a better perspective of their structure.

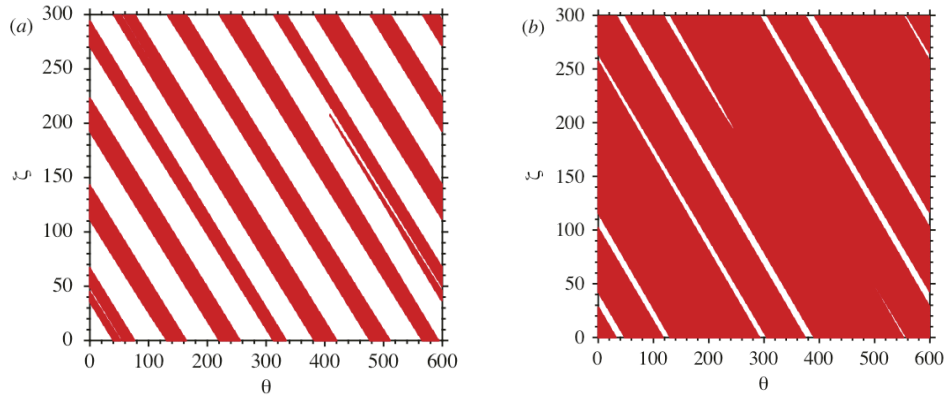

Figure 6. The connected components of the set of points for a fixed radius $r = 0.59$, where the averaged poloidal shear flow is high and at a fixed time: (a) case with no flow and $\Phi > 0$; (b) the only component in the case with flow with $\mu = 50\tau_R^{-1}$.

FIG6

At this radial position is located the singular surface 7/4. We can see the filamentary structure of the figure 6(a), it is a cycle with $m = 7$ and $n = 4$. As a consequence of the high shear flow in the second case, the Fourier component $m = 7$ and $n = 4$ and higher harmonics have been weaken due to the turbulence reduction effect by the shear flow [9], so the amplitude of the oscillation in figure 6(b) has been reduced. When this component is combined with the averaged, the Φ_{00} component, it causes the empty regions in the connected component like the case shown in figure 5(b). In figure 5, we have used a single Fourier component for simplicity. In reality there are multiple components and that makes the peaks not to be all equal. In this situation, for a given value of c, the line does not cut all peaks and instead of a cycle we will have

a broken filament, as we discussed in Ref. [3]. This is the situation of figure 6(b), the empty regions do not reproduce the full cycle structure as was the case of figure 6(a). As a consequence the toroidal knot structure of figure 6(b) is not a cycle with $m = 7$ and $n = 4$, but a cycle with $m = 3$ and $n = 2$.

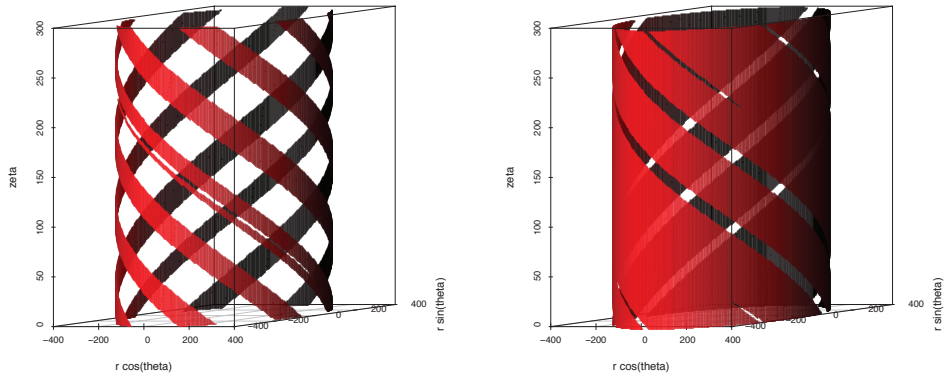

FIG7

Figure 7. The same two components as in figure 6 but plotted as 3-D structures.

So in the case with average flow and for components in which the Φ_{00} component is large the number of points of the connected component is very large and the mode number associated with the topological structure do not have to have a direct relation with the magnetic helicities that are close by. In figure 8, we can see that in a time sequence of connected components. The connected components shown in this figure are for four successive times at the radial position $r = 0.60$. The m and n values associated with the toroidal knots vary from time to time.

In any case, the new flow structures are also responsible for the trapping of particles. We discuss the particle trapping in section 8. This trapping is caused by the combination of the global shear flow and the turbulence vortices. They are local transport barriers created by the shear flow of the averaged poloidal flow. They correspond to large values of the electrostatic potential and we will call them mini transport barriers to distinguish them from the structures associated with the vortices and from the large transport barriers formed when transition to a high confinement mode. The two types of flow structures that we have identified can both be linked to the trapping of particles.

One way of estimating the importance of the change of structures introduced by the averaged velocity is to look at the distribution of the sizes of the connected components. For each radius, we select the largest size of a connected component at this radius during the time evolution. The distributions of sizes for the cases with and without averaged velocity are compared in figure 9.

We can see that for the case without averaged velocity there are no connected components with more than 90000 points. However, for the case with average velocity and $\mu = 50\tau_R^{-1}$, 47.6% of the components have a size larger than 90000 points and 25.7% have the maximum possible size, 180000 points. For the case of $\mu = 5\tau_R^{-1}$, these values increase to 76.6% and 45.5% respectively. These large size connected components correspond to the cycles that we have identified with the local shear flow induced barriers, see figure 2. Therefore, there is a strong reduction of the mid size components linked to a defined singular surface and a strong increase of the components linked to the mini barriers. For the case $\mu = 5\tau_R^{-1}$ the latter are totally

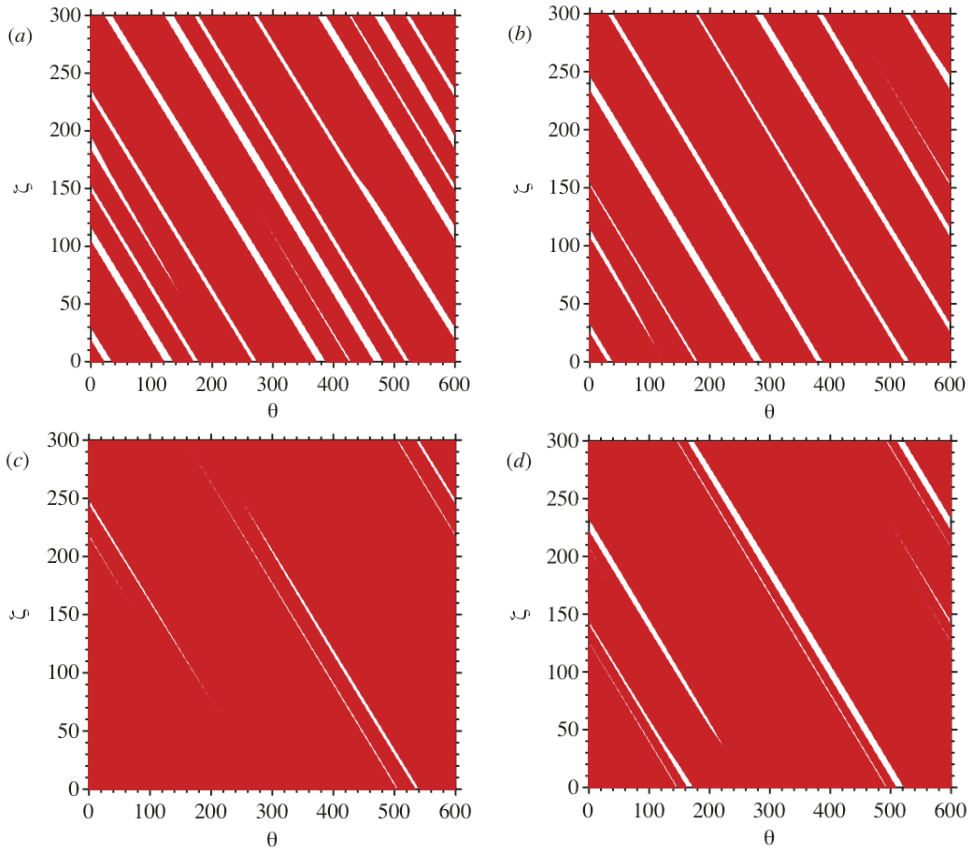

Figure 8. A time sequence of connected components. The connected components are for four successive times separated by time intervals of $5\times10^{-4}\tau_R$ at the radial position $r = 0.60$.

FIG8

dominant.

Naturally if we choose sets of points for large values of Φ_0 we would see the emergence of the filamentary structures on the regions with the mini transport barriers. In figure 5(b), we can see that if we choose $c = 0.8$, we would obtain a set similar to the one in figure 5(a). However, because the value of Φ_0 is so large, the role of these filamentary structures in the trapping is small.

6. Radial variation of the flow structures

sec:RadialChange

We have seen for the case with an averaged poloidal flow the formation of multiple mini transport barriers. This is due to the existence of radial zones with high shear flow and leads to a self-organisation of the averaged pressure profile. The result of the self-organisation is that, although the high shear flow in some radial regions reduces the level of the turbulent fluctuations, in other regions the local fluctuations may be enhanced by a local increase of the pressure gradient. In this section, we will discuss some of these alternative possibilities.

We can look at the radial region $0.566 < r < 0.633$, figure 10. In this region are

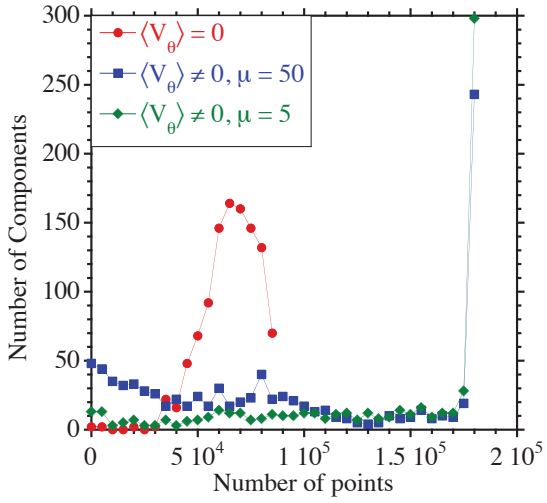

Figure 9. Distributions of sizes of the connected components for the cases with and without averaged velocity.

FIG9

located the singular surfaces 9/5, 7/4, and 5/3. We can see that the 7/4 surface is in a high shear flow region while the 9/5 and 5/3 are in low shear.

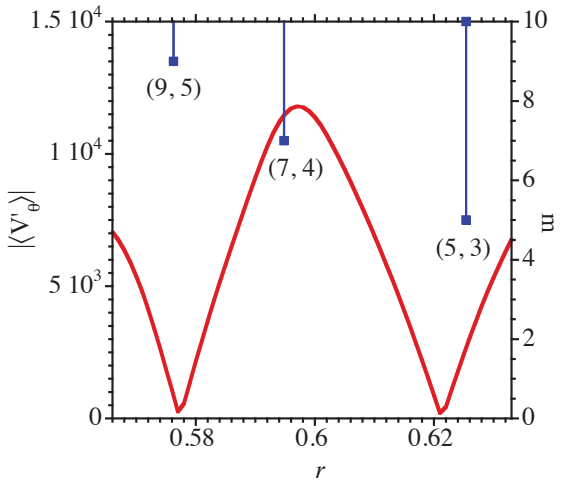

Figure 10. Radial derivative of the averaged poloidal flow in the radial region $0.566 < r < 0.633$. The location of the singular surfaces 9/5, 7/4, and 5/3 is also shown in the plot.

FIG10

In figure 11, we have plotted the connected component of Φ near the radial location of the 9/5 singular surface for the cases with and without averaged flow.

We can see from figure 11 that the $(9, 5)$ component has been reinforced in the case with flow and the topological structure has gone from a broken filament to a clean cycle. From figure 6, we already have seen that the $(7, 4)$ component was reduced and the topological structure is totally changed due to the mean flow. Finally, the $(5, 3)$ component has hardly been changed and we have the same topological structure for

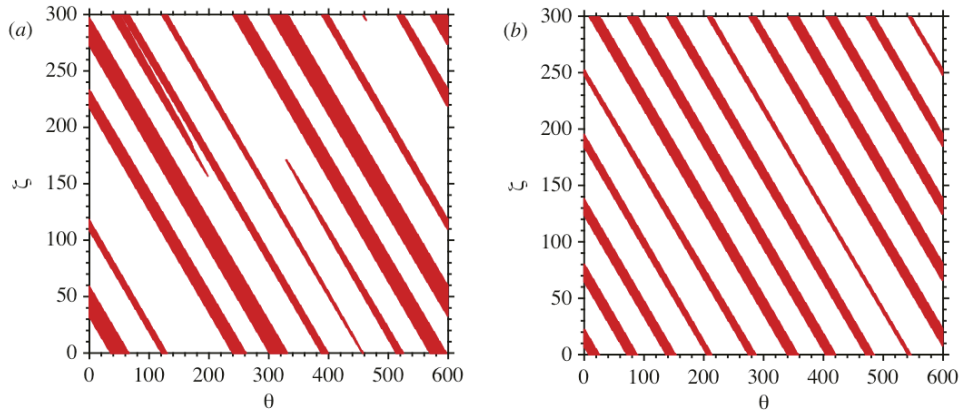

Figure 11. Connected components of Φ near the radial location of the 9/5 resonant surface for: (a) a case without averaged poloidal flow and (b) a case with averaged poloidal flow.

FIG11

both cases. Therefore all kinds of changes are possible depending on the relative position of the resonant surfaces to the location of the high shear flow regions of the averaged poloidal flow.

There are other possible changes that the averaged poloidal flow may induce in the topological structures of the flows. The presence of a poloidal flow can distort some of the turbulent flow structures. One example can be found in the region in between the 9/5 and 7/4 singular surfaces. If we look at the radius $r = 0.59$ at four different times in the time evolution, figure 12, we can see that in the first time plotted the structure is a clean cycle with $m = 9$ and $n = 5$. However in the next times a merger of two close filaments changes the structure to a combination of two cycles, one $m = 7$ and $n = 4$ and the other $m = 2$ and $n = 1$. After a period of time, the cycle goes back to $m = 9$ and $n = 5$.

7. Statistical measurements

sec:CompAnalysis

When we study the flow structures, the two measurements that we normally carry out are the length of the broken filaments and the life of the cycles. For the case without averaged poloidal velocity, both distributions seem to be well described by a lognormal distribution. When we allow the development of the averaged poloidal velocity the number and lengths of the broken filaments do not change much and the probability distribution function (PDF) of the lengths is very similar to the case without averaged velocity as can be seen in figure 13. As mentioned in section 4, we use the number of points of the skeleton of the filaments as a measure of their length. The broken filaments are mostly located away of the regions of high shear poloidal flow, so it is not surprising that their properties do not change much.

The situation seems to be different for the cycles. The number of cycles increases when we have an averaged velocity. This increase is mainly due to the new type of cycles discussed in section 5. When we look in both calculations at an interval of time of $0.03\tau_R$, we see that for the case without average flow the percentage of cycles with life equal or longer than $0.03\tau_R$ is 3.5%. However for the calculation that includes an average flow with $\mu = 50\tau_R^{-1}$ the percentage increases to 19%, and for the case with

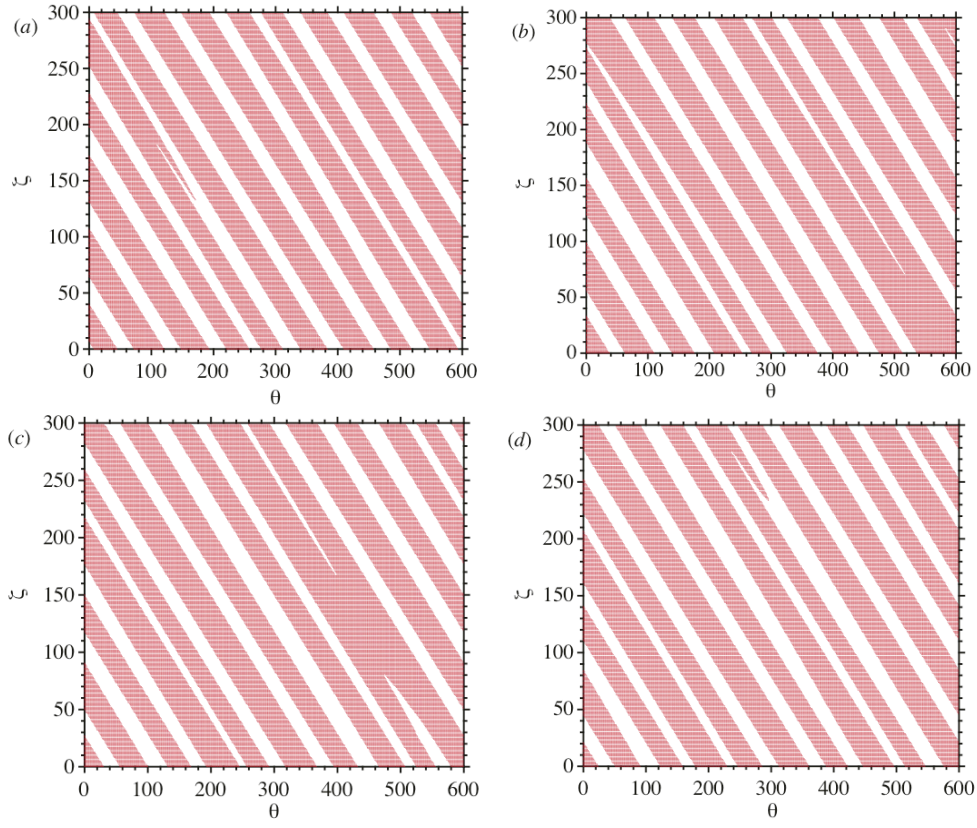

Figure 12. A time sequence of connected components. The connected components are for four successive times separated by time intervals of $5\times10^{-4}\tau_R$ at the radial position $r = 0.59$.

FIG12

$\mu = 5\tau_R^{-1}$ up to 69%. For the same time period, we have evaluated PDFs of cycle life using the Kaplan-Meier method [10] to take into account the lives that are not completed in this time interval. The results are shown in figure 14. The functional dependence of the PDF is similar in both cases. For $\mu = 5\tau_R^{-1}$, the topological structures are mostly long-living cycles. There are very few broken filaments and most cycles live longer than the calculation time, so there is not enough statistics to calculate the PDFs.

As we indicated above, most of the long living cycles in the case with $\langle V_\theta \rangle \neq 0$ are the ones created by this averaged velocity, the cycles linked to the transport barriers. This can be seen in figure 15, where we have plotted the distribution of maximum size of a component in the sequence of a life for cycles that have completed their lives in the time interval considered here with the ones that the life is not complete. The last ones include the cycles that are present during the whole interval of time.

We can see that the complete lives, which dominate the PDF shown in figure 14, are clearly dominated by the small size cycles; these are the filamentary cycles, while the very large ones dominate the incomplete lives. Note that the size of the component is measured in cubes and with the resolution that we are using for each component, 300×600, the size of a full component is 180000. These large components correspond

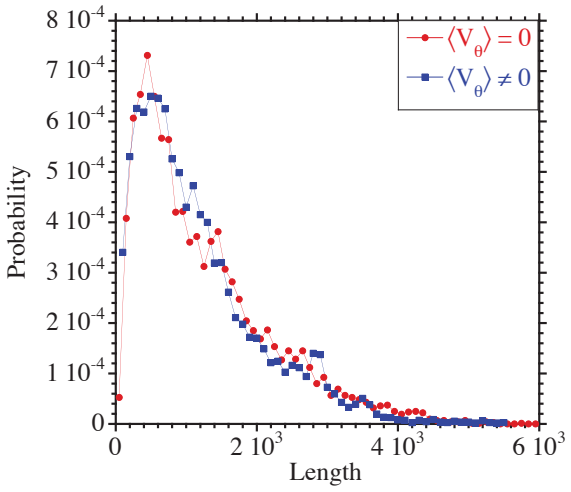

Figure 13. Probability distribution function of the lengths of the broken filaments for: (a) a case without averaged poloidal flow and (b) a case with averaged poloidal flow with $\mu = 50\tau_R^{-1}$.

FIG13

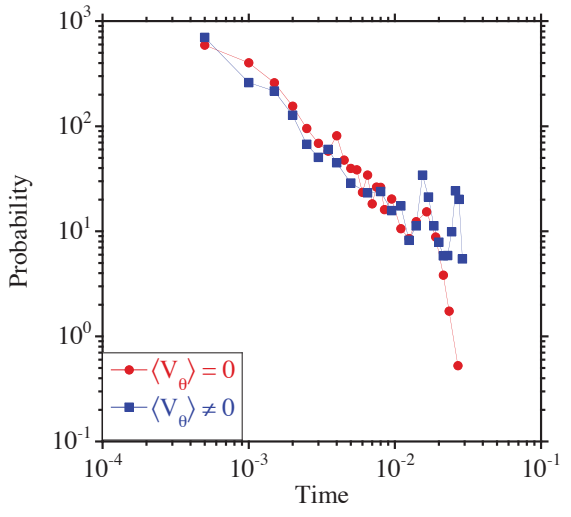

Figure 14. Probability distribution function of the lives of the cycles for: (a) a case without averaged poloidal flow and (b) a case with averaged poloidal flow with $\mu = 50\tau_R^{-1}$.

FIG14

to the cycles generated by the averaged poloidal flow that create the transport barriers. Therefore, the comparison of the life of cycles in figure 14 is essentially for filamentary cycles, so it is not surprising that the distributions are similar.

Another way of looking at the long living cycles is by their radial position. For the case without averaged poloidal flow, cycles living $0.03\tau_R$ or longer are associated with two of the low resonant surfaces, the 1/1 and the 5/3, as can be seen in figure 16(a). However, for the case with averaged poloidal flow there are the ones associate with these resonant surfaces but there are many more distributed over most of the radius,

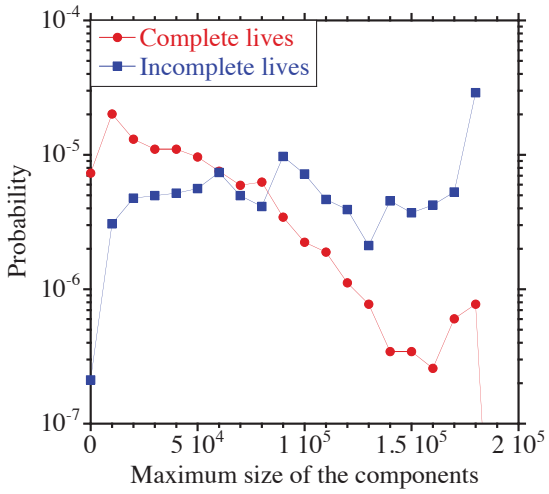

Figure 15. Distribution of maximum size of a component in the sequence of a life for cycles that have completed their lives in the time interval $10^{-3}\tau_R$ and for the ones that the life is not complete in the same time interval.

FIG15

as shown in figure 16(b). The latter are the mini transport barriers.

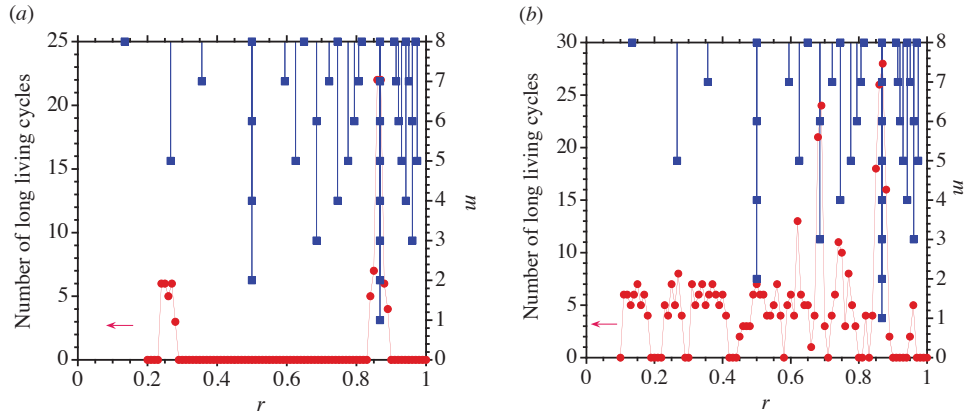

Figure 16. Radial position of the long living cycles for: (a) a case without averaged poloidal flow and (b) a case with averaged poloidal flow with $\mu = 50\tau_R^{-1}$. They are also plotted the radial positions of the low m resonant surfaces.

FIG16

8. Impact of the flow structures in tracer transport

sec:PartTrapping

To better understand the effect of the flow structures on transport, we consider a set of tracer particles moving with the turbulent flow. The equation of the tracer motion is

$$\frac{\mathrm{d}\mathbf{r}}{\mathrm{d}t} = -\frac{\nabla_\perp \Phi \times \mathbf{z}}{B_0} + V_0 \mathbf{b}, \qquad (18)$$

eq:tracer

where $\mathbf{r} \equiv (r, \theta, \zeta)$ is the tracer position, and $\mathbf{b}$ is the unit vector in the direction of the magnetic field.

In equation (18), V_0 is a constant velocity along the magnetic field lines. If $V_0 = 0$, Φ is a Hamiltonian-like constant of motion. However, for $V_0 \neq 0$, Φ is not conserved and particle tracers can be lost out of the confinement region.

We start the calculation with 10^5 particle tracers at time equal 0, and follow their motion up to one resistive time. In figure 17, we show the time evolution of the number of tracers for a case with no averaged poloidal velocity and for the case with averaged poloidal velocity with $\mu = 50\tau_R^{-1}$. None of the tracers is lost within this time interval for the case with $\mu = 5\tau_R^{-1}$. The tracers move with $V_0 = 500R_0/\tau_R$ for the three cases.

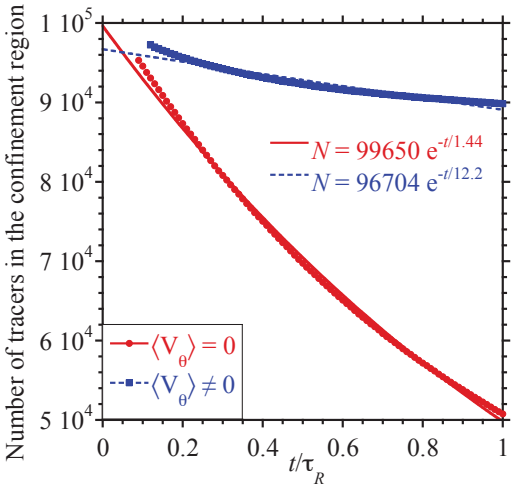

Figure 17. Number of tracers in the confinement region as a function of time for a case without averaged poloidal flow and a case with averaged poloidal flow with $\mu = 50\tau_R^{-1}$.

FIG17

We can see the increase in confinement in the case with averaged poloidal velocity. By fitting the number of particles as a function of time with an exponential function, we can estimate the particle confinement time, which is $1.44\tau_R$ for the case with no averaged poloidal velocity and $12.2\tau_R$ for the case with averaged poloidal velocity. Therefore, in the second case, there is an enhancement of the confinement time by a factor of 8.5.

The confinement improvement is due to the formation of the mini transport barriers. There is an increase in the tracer trapping by these barriers. To see the change in the characteristic properties of the trappings when there is an averaged poloidal flow we calculate the slope in the $\theta - \zeta$ plane of the tracer trajectory during the trapping phase. If the tracers follow the flow filaments linked to the magnetic field lines the slope should be $-q$. This is the case for the tracers in the turbulence without averaged poloidal flow because they always follow structures like the one shown in figure 6a. However, the slope of the tracer trajectory when they are trapped may be very different when a poloidal flow is present, because they are trapped in the more complicated flow structures described in section 5. This difference in the properties of trapping is illustrated in figure 18, where we plotted the distribution of the slopes of

the tracer trajectories when trapped for the two flow configurations considered here.

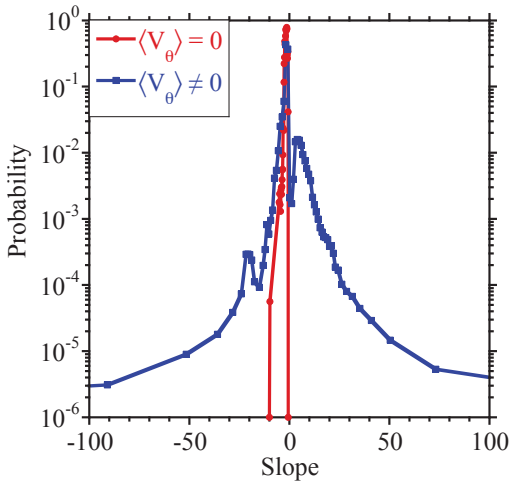

Figure 18. Distribution of the slopes of the tracer trajectories when trapped for a case without averaged poloidal flow and a case with averaged poloidal flow with $\mu = 50\tau_R^{-1}$.

FIG18

This shows the role played by the mini transport barriers in increasing the trapping of the tracer particles. A more detailed analysis of the properties of the trappings in both situations will be given elsewhere.

9. Conclusions

sec:Conclusions

The present analysis of plasma flow structures is based on the dynamics of the resistive pressure-gradient-driven turbulence in the electrostatic approximation. The calculations were done well below the ideal ballooning instability threshold. The analysis is an extension of the one done in Ref. [3] for the case that no averaged poloidal flow was included in the calculation.

The presence of a significant averaged poloidal flow in the plasma changes the topological structures of the turbulent flow. Without the averaged flow, the turbulent structures are filamentary and linked to the low rational surfaces. When the averaged poloidal flow is present and in the region of the high shear flow the structures are essentially toroidal with some deformations.

The high shear flow regions are associated with these large structures of the electrostatic potential. They create barrier like structures that trap the particle. We have called these structures mini transport barrier to distinguish them from the transport barriers that cause the transition to high confinement regime.

The mini transport barriers are in general long living structures with live time only comparable to the lives of the cycles at the very low resonant surfaces like the 1/1.

Acknowledgments

This research was sponsored by DGICYT (Dirección General de Investigación Científica y Técnica) of Spain under Project No. ENE2012-38620-C02-02. One of us (BAC) also gratefully acknowledges the support from a "Cátedra de Excelencia" from Universidad Carlos III and Banco de Santander.

References

Montroll [1] Montroll E W and Weiss G 1965 *J. Math. Phys.* **6** 167
Sanchez [2] Sanchez R, Carreras B A and van Milligen B Ph 2005 *Phys. Rev.* E **71** 011111
Carreras3 [3] Carreras B A, Llerena Rodríguez I and García L 2013 *J. Phys. A: Math. Theor.* **46** 375501
Strauss [4] Strauss H R 1977 *Phys. Fluids* **20** 1354
Carreras2 [5] Carreras B A, Lynch V E, Garcia L and Diamond P H 1993 *Phys. Fluids* B **5** 1491
Carreras4 [6] Carreras B A, Lynch V E, Garcia L and Diamond P H 1995 *Phys. Plasmas* **2** 2744
Iiyoshi [7] Iiyoshi A et al. 1999 *Nucl. Fusion* **39** 1245
Skeleton [8] Gonzalez R and Woods R 2008 *Digitsal Image Processing* (3rd Ed.) Prentice Hall
Biglari [9] Biglari H, Diamond P H and Terry P W 1990 *Phys. Fluids* B **2** 1
Kaplan [10] Kaplan E L and Meier P 1958 *J. Am. Stat. Assoc.* **53** 457